Dynamic response of commuter category aircraft wing against drone collision

Budi Aji Warsiyanto[1], Muhammad Hadi Widanto[1], Ilham Musthofa[1], Ichsan Maulana[1]

[1]Faculty of Aerospace Technology, Air Marshal Suryadarma University, Indonesia

e-mail: budiajiwarsiyanto@gmail.com

Received: 30-12-2020. Accepted: 16-03-2021. Published: 30-06-2021

Abstract

The extensive application and development of drones provides high potential airborne collision between manned aircraft and civil Unmanned Aerial Vehicles (UAVs) or known as drone. This phenomenon is a serious threat to aircraft operation safety. The objective of this paper is to investigate the dynamic response of the aircraft wing section commuter category when experienced the drone collision. The 'Mavic' drone with a mass of 735 g was used as an impactor in simulation. Explicit dynamic code ABAQUS was employed to simulate the collision process based on the difference of collision scenarios to assess the hazard. The results showed that 735 g drone collision at the aircraft maximum approach flap speed and cruising speed could cause some damage on the wing front spar. The 735 g drone collision is more serious than 910 g bird strike providing information that component hardness plays an important role in wing damage. Furthermore, the potential source of ignition may be caused by the lithium-ion battery penetrated the airframe.

Keywords*: drone collision, damage assessment, wing section, finite element method.*

Nomenclature (Optional)

σ	=	stress, MPa
ε	=	strain, -
ν	=	poisson's ratio, -
E	=	elastic modulus, GPa
ρ	=	density, kgm^{-3}
G	=	shear modulus, GPa

1. Introduction

Aircraft components are vulnerable to collision from foreign objects such as debris, hail, or bird strike. The flight safety operations of civil aircraft are under threat from these collision incidents and may cause catastrophic accidents. Nowdays, the rapid growth in UAVs makes the impact scenarios even more complicated. (Jenkins & Vasigh, 2013) estimates that the total UAV market will grow to a total economic impact of $82.1 billion by the end of 2025. The airworthiness verification of aircraft structure in facing of drone collision has not been taken into account in its design process. That is, the possibility of impact between aircraft and UAVs exists, whereas its safety risk is unknown. So, evaluations of collisions between UAVs and commercial aircraft are necessary to minimize future damage.

The background of this research is because there are no regulations governing the airworthiness of a drone collision. In addition, up to now, there is no collision simulation between the drone and the commuter wing leading edge for commuters that could be found in published reports. Several published reports such as (Song et al., 2017)(Schroederi et al., 2017) investigated the dynamic response of a high-bypass engine during drone ingestion, different risk levels were classified and a comparison with

bird ingestion. (Meng et al., 2019) performed a collision simulation between a structure level drone and a commercial airliner horizontal stabilizer section to investigate the dynamic response of primary operation components with PAM-CRASH code. (Lu et al., 2020) performed a collision simulation using numerical and experimental between drones and nose aircraft. The research shows the configuration, material, weight, speed, and attitude of drones have significant effects on the impact damage to the windshield.

Based on the explanation of the paragraph above, this research performed a numerical test of the drone collision on the component of the wing section of the commuter category aircraft. The drone with 735 g was used as projectile and a section of a commuter category aircraft wing was employed as the target specimen. The objective of this paper is to investigate the dynamic response of the aircraft wing section when experienced the drone collision and compare it with the effects of bird strike and drone collision. Thus, it can be seen the ability of the wing structure to withstand the impact loads due to drone collisions and bird strikes. In addition, the difference in damage between the drone collision and bird strikes can be obtained. The investigations are performed numerically using the finite element method.

2. Methodology

2.1. Method

Drone collision experimentally provides a direct method to evaluate the damage severity but the high cost of the test makes it's challenging to enumerate all collision scenarios. With the finite element method (FEM), the collision scenario will be more efficient. Drone collision ground test still needs to be conducted to validate numerical simulations. However, due to limited equipment, testing was only carried out numerically. The collision simulations in this study were performed by explicit dynamic finite element solver ABAQUS. The simulation model was performed based on the difference of impact scenarios such as drone attitude (impact angle) and impact velocity to evaluate the damage severity. Comparison with bird strike was also performed in this paper.

2.1.1 The drone

The drone model used in this study has a geometry similar to 'Mavic' supplied by DJI. General size of the drone was about 435*517*70 mm and the total weight (with camera) was 735 g. This mass was close to the bird mass required by the bird strike resistance certification for airframe, namely 910 g. Geometric features and some minor components were eliminated in modeling but their mass was added to the main structure to keep the total mass and center of gravity unchanged. The thin-walled structures such as the frame, propeller, and electronic board were modeled by shell elements, whereas the battery, motors, and camera were modeled by solid elements. The drone's materials and mass distribution are shown in Figures 2-1a and 2-1b. Based on a mesh convergence study in Subsection 2.3.3, the average element size for overall components was 3 and 5 mm as shown in Figure 2-2. The mesh size of 5 mm for frame, propeller, electronic board, battery, and motors, whereas the camera has the mesh size of 3 mm because the geometric is smaller than others component. Overall, the drone model consists of 8,681 shell elements and 2,832 solid elements.

2.1.2 The commuter aircraft wing

The outer wing structure has a length of 2,000 m is used as the target in the impact simulation. The swept angle of the wing was 3.5° and the impact direction was along the aircraft's flight path. The wing mass was 21.81 kg consisting of skin, 11 ribs, and 2 spars fixed to the root as shown in Figures 2-3a and 2-3b. Each component on the wing is modeled with a shell element, S4R. The local mesh is employed on the wing, which is 10 mm in the impact area and larger in the area far from the impact as shown in Figure 2-3c resulting in 68,919 elements. Tie constraints are employed to simulate the rivets joining between skin and ribs and skin and spars.

2.1.3 Constitutive model for materials

The aluminum alloy 2024-T3, 6061-T6, and polycarbonate (PC) were implemented by incorporating isotropic hardening using the Von Mises yield criterion. The mechanical properties of aluminum alloy 2024-T3, 6061, and PC are investigated by ASM Inc. and DJI Technology Co., Ltd and listed in Table 2-1. Von Mises is a simple and convenient criterion to apply as it defines a smooth and continuous yield surface with good approximation at high stresses (Dar et al., 2013). At given principal stresses σ_1, σ_2, and σ_3, the yield criterion is defined as

$$(\sigma_1 - \sigma_2)^2 + (\sigma_2 - \sigma_3)^2 + (\sigma_1 - \sigma_3)^2 = 2{\sigma_y}^2 \quad (3\text{-}1)$$

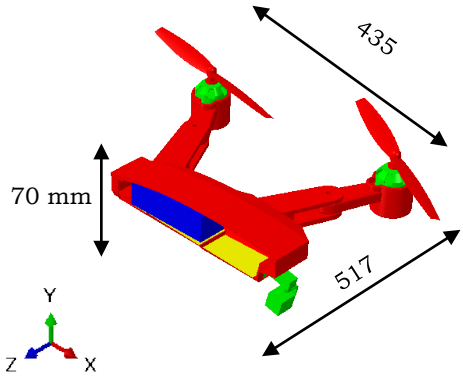

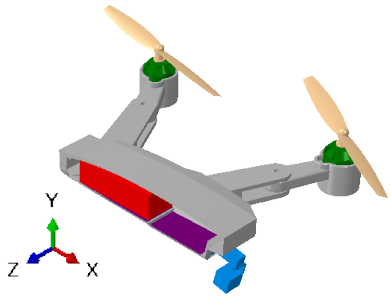

Code	Material
	Polycarbonate
	Lithium-ion
	6061-T6 aluminum alloy
	Glass-epoxy

(a)

Code	Component	Mass (g)
	Frame	237
	Motor	223
	Battery	119
	Electronic board	94.1
	Camera	26.5
	Propellers	35.4
Total		735

(b)

Figure 2-1: (a) Drone materials and (b) mass distribution

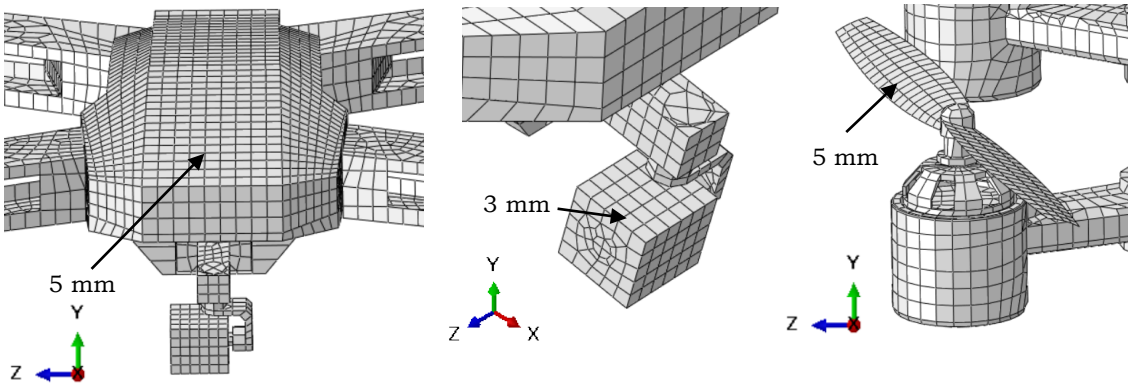

Figure 2-2: Drone element size

The maximum principal strain criterion implies that if the maximum tensile principal strain exceeds the prescribed limits, then the material will instantaneously fail. Failure is predicted when either of the principal strains ε_1 or ε_2, resulting from σ_1 or σ_2, equals or exceeds the maximum strain ε_f corresponding to the yield strength σ_y of the material in uniaxial tension or compression. For yielding in tension the minimum principal strain ε_1 would equal the yield strain in uniaxial tension (Dar et al., 2013). If the strains are expressed in terms of stress, then

$$\varepsilon_1 = \frac{\sigma_1}{E} - \frac{\nu}{E}(\sigma_2 + \sigma_3)$$
$$\sigma_y \geq \sigma_1 - \nu(\sigma_2 + \sigma_3) \quad (3\text{-}2)$$
$$\varepsilon_f = \varepsilon_t - \frac{\sigma_t}{E}$$

The mechanical properties of the glass-epoxy composite were measured by (Waqas et al., 2019) as shown in Table 2-2. Based on the study of (Sahraei et al., 2012)(Sahraei et al., 2014), the cells of lithium-ion batteries and a 60% porosity of the active particles are constructed with crushable foam material in the first approximation, which the mechanical properties are shown in Table 2-3.

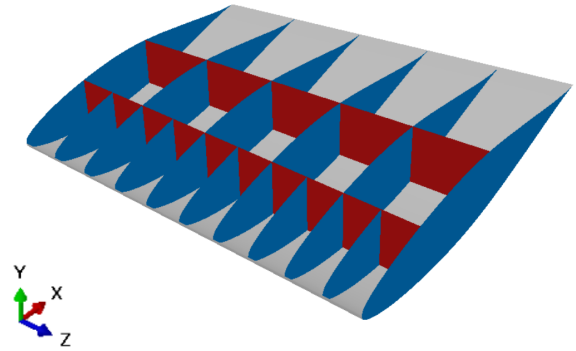

Code	Component	Thickness (mm)
	Skin	0.6
	Spar	1.2
	Rib	0.6

(a)

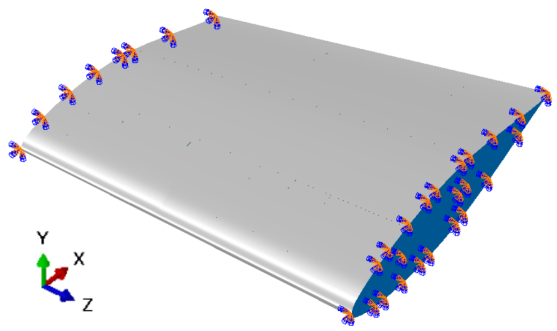

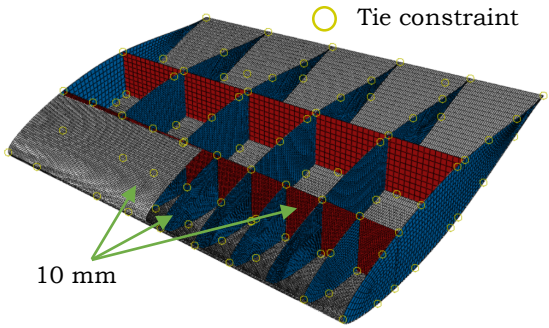

(b) (c)

Figure 2-3: (a) Geometric details, (b) boundary conditions, and (c) element size of the wing

Table 2-1: Mechanical properties of the material

	Density ρ (kgm^{-3})	Elastic modulus E (GPa)	Poisson's ratio ν	Yield stress σ_y (MPa)	Ultimate stress σ_u (MPa)	Failure strain ε_{max}
2024-T3	2,780	73.1	0.33	345	483	0.18
6061-T6	2,700	68.9	0.33	276	310	0.12
PC	1,180	6.2	0.3	62	75	0.2

Table 2-2: Mechanical properties of glass-epoxy

Density ρ (kgm^{-3})	Elastic modulus E_1 (GPa)	Elastic modulus E_2 E_3 (GPa)	Shear modulus G_{12} G_{13} (GPa)	Shear modulus G_{23} (GPa)	Poisson's ratio ν_{12} ν_{13}	Poisson's ratio ν_{23}
2000	45	10	5	3.85	0.3	0.4

Table 2-3: Mechanical properties of the battery

Density ρ (kgm^{-3})	Elastic modulus E (GPa)	Poisson's ratio ν
1,750	0.5	0.01

2.1.4 Computational model

To obtain a balance between accuracy and computational efficiency was performed a mesh sensitivity study. Drone component, i.e motor was impacted to an aluminum alloy 2024-T3 skin of wing at a velocity of 80 ms-1. The mesh sizes of the skin were 30 mm, 15 mm, 10 mm, 7 mm, and 5 mm. The internal energy of the skin was employed as the criterion which is shown in Figure 2-4. It can be seen that the performances of the FE models were almost identical when the mesh size was below 10 mm which equals 45,200 elements. Finally, an average element size of 10 mm was employed in this research.

The dynamic explicit analysis was employed in this simulation because of its effectiveness to solve highly non-linear problems. The critical time step was 1*10−5 s to capture all energy associated with the stress wave propagation during the impact process. The friction behavior between the drone and the wing was set to be 0.26 based on a material handbook. The skin, spar, and rib structure are modeled using a 4-node shell continuum (S4R) element with 5 integration points along the direction of the element thickness. Hourglass control with enhanced is used to prevent artificial zero energy deformation mode. Additionally, the integration point is used to prevent volumetric locking during impact. General contact was employed to define all contact's behavior for each component.

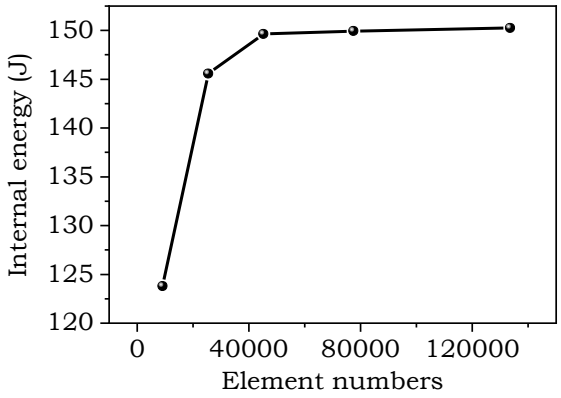

Figure 2-4: Mesh convergence study

3. Result and Analysis

3.1. Different impact location and drone attitude

Variation of simulations was performed to study the effect of different impact locations and drone attitudes on the dynamic response of the wing and determine the most serious scenario to damage the wing structure. The impact velocity was used to the simulations of different impact location and drone attitude was 80 ms^{-1}. This impact velocity was relative value which consists of the drone's maximum velocity of 18 ms^{-1} and aircraft velocity of 62 ms^{-1} at the aircraft maximum approach flap. The aircraft velocity was chosen because the airworthiness regulations for bird strikes, namely CASR 23.775 (Republic Indonesia Ministry of Transportation, 2014) set the impact parameter for commuter aircraft was a 910 g bird when the velocity of the aircraft is equal to the aircraft's maximum approach flap speed. Two locations of impact were analyzed, namely on the rib and between ribs as shown in Figure 3-1a. Figure 3-1b shows that there was global deformation at the leading edge of the wing and that there was no serious damage to the wing structure when the impact location was on the rib. However, when the impact on between the ribs, the drone broke the skin and hit the front spar so it is considered to be more serious than the rib situation. Figure 3-2 shows the wing internal energy for the difference in collision, that is, on the rib and between the ribs. It is seen

that the internal energy between the ribs is lower than collision on the ribs. This is due to when the collision on between the ribs, the skin structure fails so that the energy absorbed by the deformation is lower than the collision on the rib (no damage and the wing structure absorbs energy by deformation).

Different drone attitudes (impact angle) were also simulated, while the center of gravity of the drone was not changed. The attack angle varied from −45° to 45° at an interval of 22.5°. The impact scenarios were marked #1−#5 as shown in Figure 3-3. The principal strain of the wing was employed as the criterion to evaluate the impact consequences. Based on Figure 3-4, it can be assumed that the drone with no attack angle (0˚) would cause the plastic strain reaches a value equal to the strain failure. This is supported by Figure 3-5 which shows the comparison of internal energy of wing for different drone attitudes. As explained by the difference in impact location (on rib and between rib), the internal energy with no attack angle (0°) has the lowest value because the skin structure fails so that the energy absorbed by the deformation is lower than others scenario.

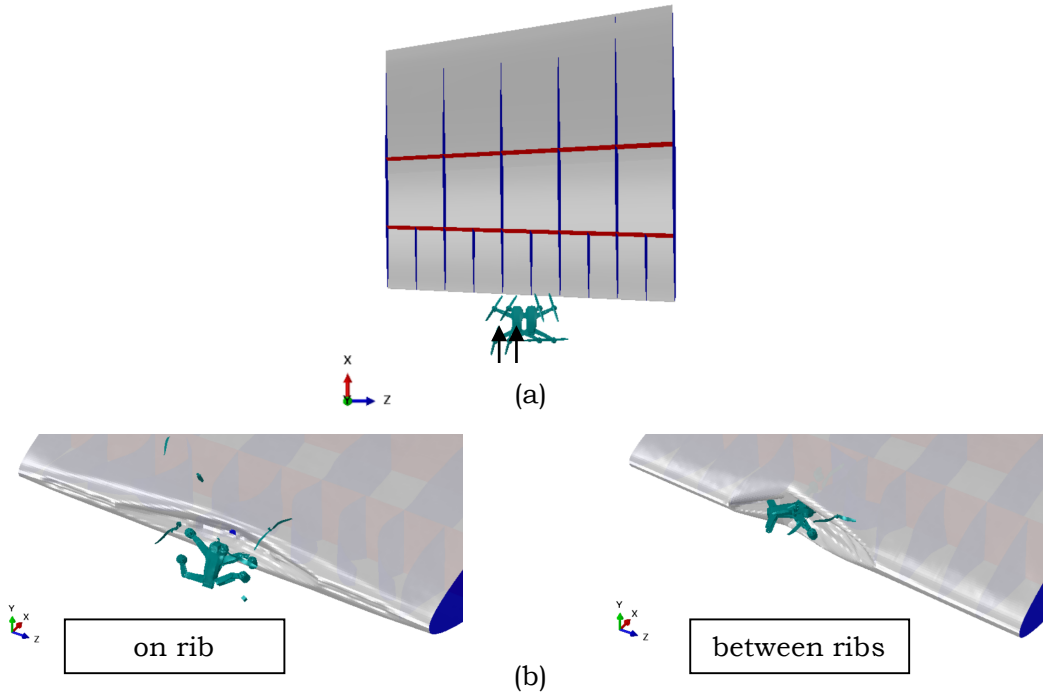

Figure 3-1: (a) Different impact locations and (b) damage characteristics

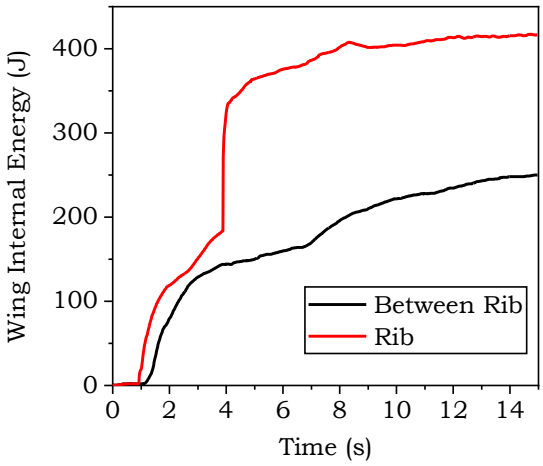

Figure 3-2: Wing internal energy during the drone collision on between rib and rib

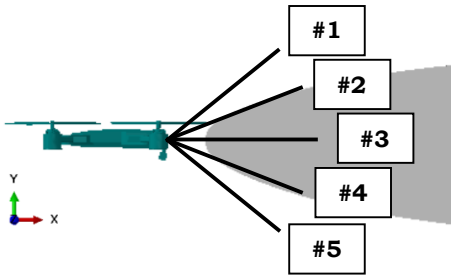

Figure 3-3: Different drone attitudes

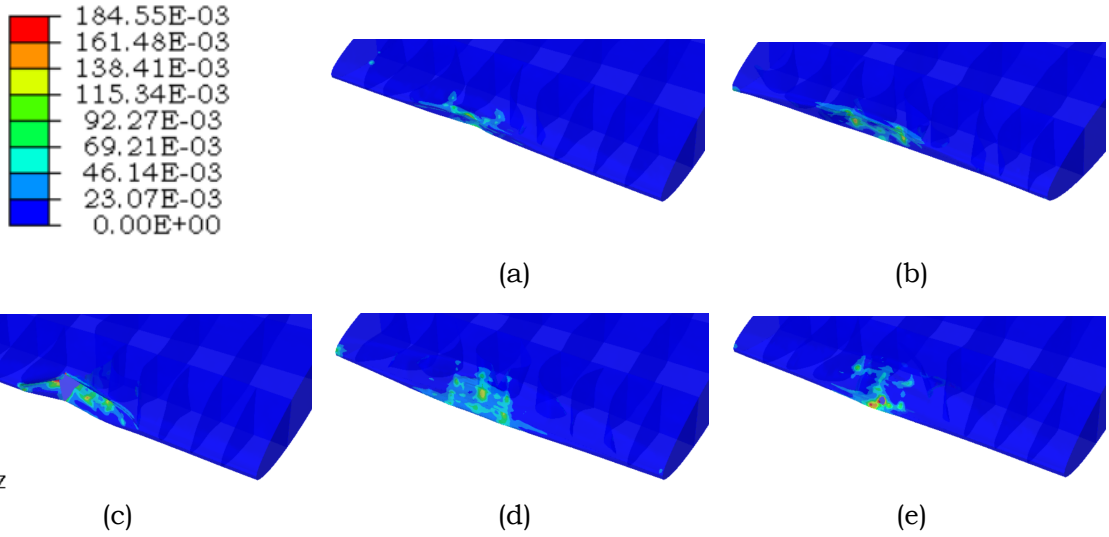

Figure 3-4: The plastic strain at impact angle (a) 45˚, (b) 22.5˚, (c) 0˚, (d) -22.5˚, and (e) -45˚

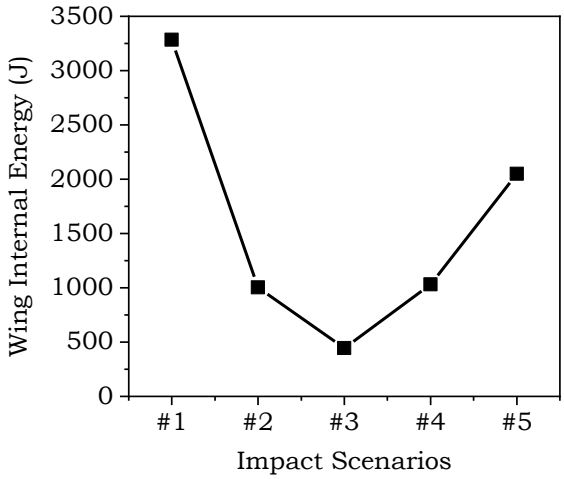

Figure 3-5: Comparison wing internal energy for the different drone attitudes

3.2. Different drone velocity

The impact velocity was varied to determine the minimum and maximum damage when the 735 g drone crashed on the wing. Three different velocities were investigated according to the following considerations. Firstly, based on (FAA, 2016), small UAVs are not permitted to be operated over 400 feet (approximate 120 m). Secondly, the maximum flight altitude of the above UAVs is restricted to be 500 m from the ground by DJI. Thirdly, (FAA, 1993) states that unless otherwise authorized by the Administrator, no person may operate an aircraft below 10,000 feet (approximate 3,000 m) MSL at an indicated airspeed of more than 250 knots. Therefore, three different velocities of aircraft

were 40 ms^{-1} at take-off (approximate 120 m), 62 ms^{-1} at approach (approximate 500 m), and 103 ms^{-1} at cruising conditions (approximate 3,000 m) are determined based on the flight envelope. The maximum flight speed of the drone was 18 ms^{-1} thus the impact velocities were 58 ms^{-1}, 80 ms^{-1}, and 121 ms^{-1}.

Figure 3-6 show the result summary of drone collision with velocity impact differences. It can be seen that at the velocity of 58 ms^{-1}, the skin is no fracture so that no drone component penetrated the structure of wing. At an impact velocity of 80 ms^{-1}, the drone broke the skin cause the maximum plastic strain exceeds the material failure strain, namely 18%. However, the front spar remained intact. At higher impact velocity, that is 121 ms^{-1}, the drone caused more fracture to the skin and damage to internal structures. The energy distribution is showed in chart form. At low impact velocity, the structural internal energy is higher than the impact velocity of 80 ms^{-1} and 121 ms^{-1}. Furthermore, the residual kinetic energy at the impact velocity of 58 ms^{-1} lower than the impact velocity of 80 ms^{-1} and 121 ms^{-1}. The drone's internal energy increases 180% when the kinetic energy was 4.35 times larger. At the impact velocities of 80 ms^{-1} and 121 ms^{-1}, the structural internal energy is lower than the impact velocities of 58 ms^{-1} because the structure failed at the initial impact so that no energy is absorbed by the deformation of the structure.

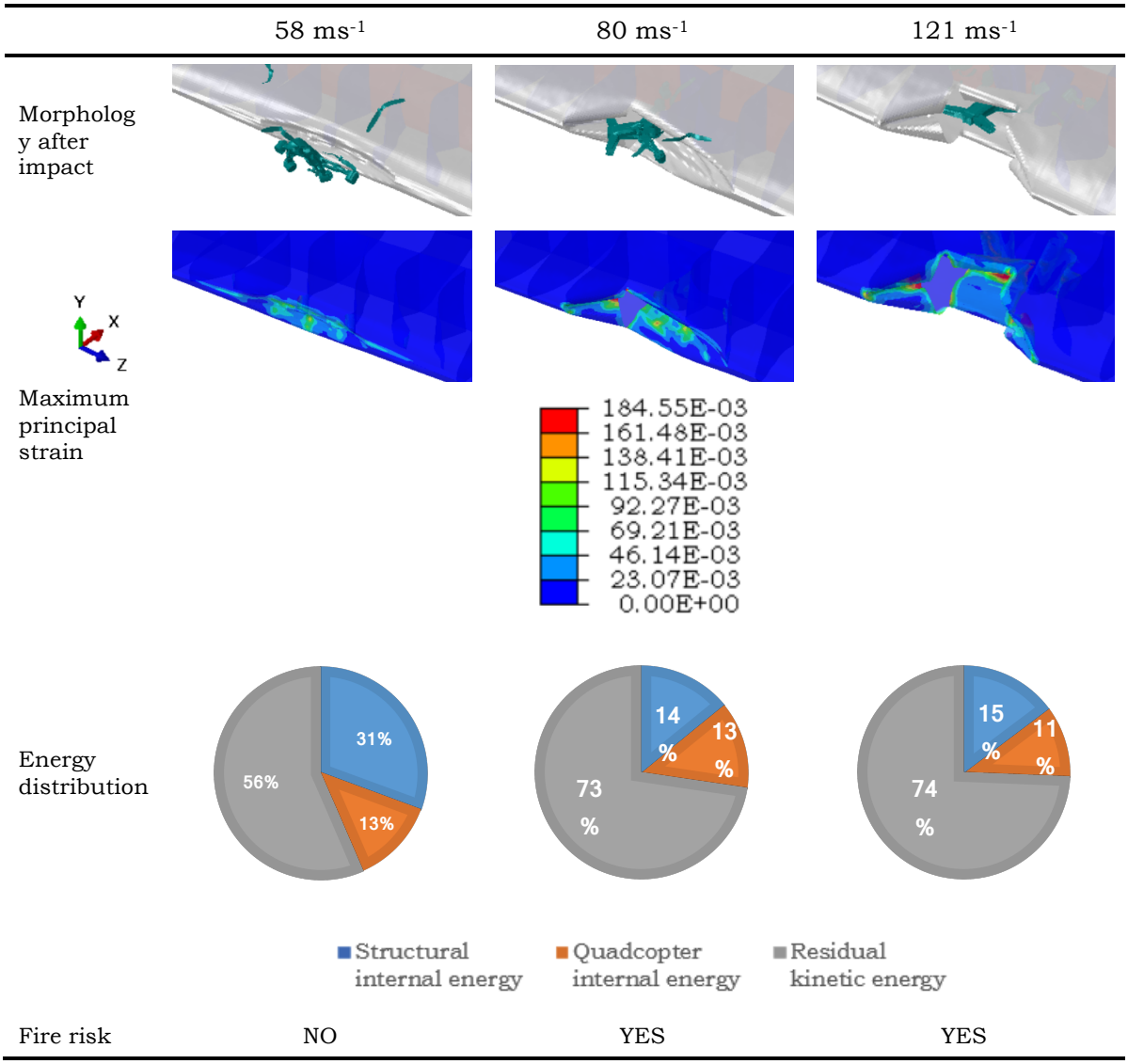

Figure 3-6: Summary chart of different drone velocities

According to the airworthiness standards, it can be assumed that at the impact velocity of 58 ms^{-1}, the aircraft could complete the flight. At the impact velocity of 80 ms^{-1}, the primary structure of the wing was not severely damaged, but the fire risk of the lithium-ion battery should be considered. However, at the impact velocity of 121 ms^{-1},

the front spar is subject to severe plastic deformation and the residual strength should be evaluated to ensure flight safety.

3.3. Comparison with a bird strike

3.3.1. Bird model

One of the methods to simulate bird was Smoothed Particle Hydrodynamics (SPH). The method was developed to overcome large mesh distortion in high-speed impact problems. Particles are nodes that connect each element obtained from the mesh. According to (Heimbs, 2011), SPH has the advantages in the accuracy and of the computation process. The same result was also obtained by (Liu et al., 2014) through a comparison between simulation results from Lagrangian and SPH model which is crashed on flat plates. (Hedayati & Ziaei-Rad, 2013) studied the effect of different bird geometries on impact results through the numerical method and obtained cylinder with hemispherical ends with a length to diameter ratio of 2 was recommended. As mentioned in Subsection 3.1, a bird with a mass of 910 g was adopted in this research based on (Republic Indonesia Ministry of Transportation, 2014). The average density of birds was 938 kgm^{-3} based on a report from (SIMULIA, 2011). The SPH bird model has 11,797 particles as shown in Figure 3-7. Note that this bird model is homogeneous that does not consider differences in bird organs such as muscles or bones and can only be used to predict the macro-response of the structure in bird strike simulations.

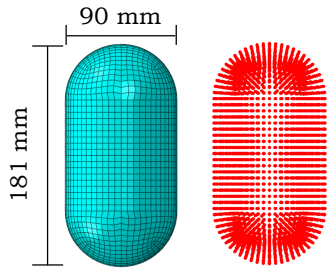

Figure 3-7: The SPH bird model

Hydrodynamics is described by the relationship of peak pressure to density ratio, known as the Equation of State (EOS) as shown in Figure 3-8. EOS considers fluid material variables, such as pressure, density, strain, and internal energy (Hedayati & Sadighi, 2015). Characteristic for bird materials during bird strike process has been investigated by (Barber & Wilbeck, 1987). (Smojver & Ivančević, 2012) employed different EOSs to study bird strikes on aircraft structures. The type of EOS used in this study is tabular based on (SIMULIA, 2011) which is formulated as follows:

$$p = f_1(\varepsilon_{vol}) + \rho_0 f_2(\varepsilon_{vol}) E_m \tag{3-1}$$

Where p and ρ_0 are the pressure and bird density at atmospheric pressure, $f_1(\varepsilon_{vol})$ and $f_2(\varepsilon_{vol})$ are the logarithmic functions of volumetric strain ε_{vol}, with $\varepsilon_{vol} = \ln(\rho_0/\rho)$, and E_m is the internal energy per unit mass. The contribution of internal energy to the pressure is usually neglected when dealing with the hydrodynamic impact. Therefore, $f_2(\varepsilon_{vol}) = 0$ and $p = f_1(\varepsilon_{vol})$. Real bird has a porosity between organs thus reducing the density which is the average density of birds ranges from 900-950 kgm^{-3} (Hedayati & Sadighi, 2015). Porosity has a significant effect on the resulting peak pressure. For example, a porosity of 0.1 can reduce peak pressures up to 50% compared to porosity of 0 (Wilbeck, 1978). In this study, a bird material with 0 porosity was employed to get conservative results. Parameters of 0 porosity are shown in Table 3-1.

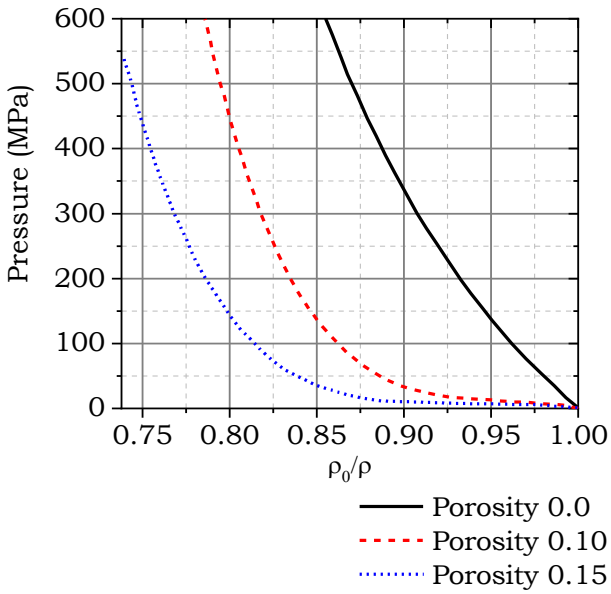

Figure 3-8: Hugoniot pressure of water-like homogenized bird materials (SIMULIA, 2011)

Table 3-1: Tabular EOS with 0% porosity parameters (SIMULIA, 2011)

No	f_1 (MPa)	ε_V	No	f_1 (MPa)	ε_V
1	0	0	14	263,29	-0,088
2	15,82	-0,007	15	289,34	-0,095
3	32,56	-0,014	16	315,39	-0,100
4	51,17	-0,021	17	342,37	-0,107
5	68,85	-0,028	18	370,29	-0,113
6	87,45	-0,035	19	399,13	-0,119
7	106,06	-0,042	20	429,83	-0,126
8	127,46	-0,049	21	460,53	-0,132
9	147,93	-0,055	22	493,09	-0,138
10	168,40	-0,062	23	526,59	-0,144
11	191,66	-0,068	24	561,01	-0,150
12	213,98	-0,075	25	595,43	-0,156
13	238,17	-0,081			

3.3.2. Result and discussion

The comparison between 735 g drone collision and 910 g bird strike is shown in Figure 3-9 (a) and 3-9 (b). The impact velocity was 80 ms^{-1} and the impact location was between ribs. During the bird strike process, the skin of the wing cut the bird body and the debris slid away from the structure, the skin suffered extensive permanent deformation but no penetration was observed. However, during the drone collision process, the drone broke the skin and penetrated the airframe, which may cause damage to the front spar. According to airworthiness standards, the drone collision was assumed to be more dangerous than a bird strike. Under the same impact velocity, the drone's kinetic energy was 81.1% of the bird's kinetic energy.

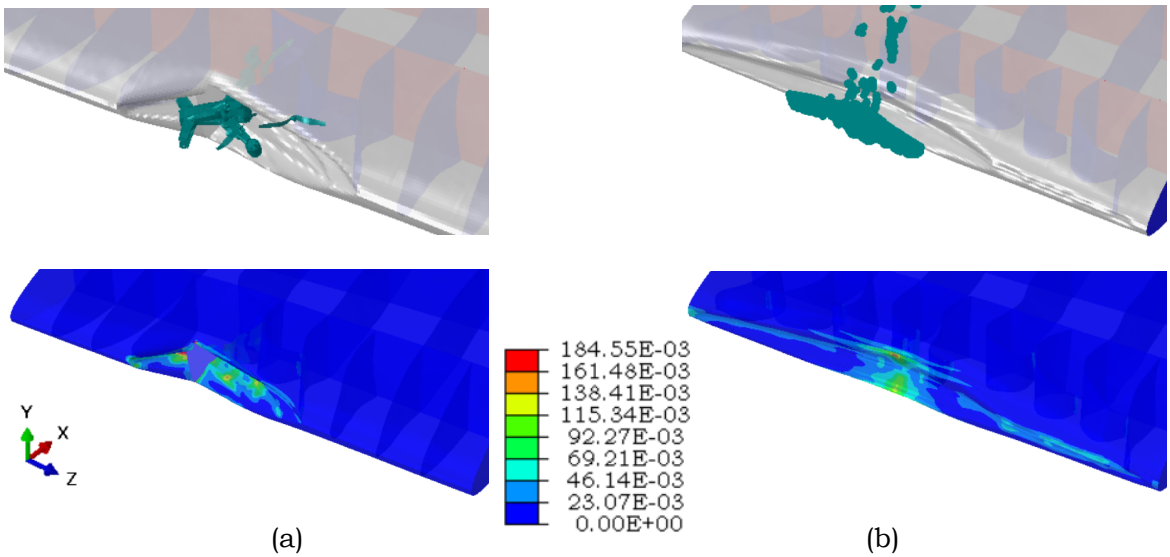

Figure 3-9: Damage characteristics of (a) drone collision and (b) bird strike

The impact level consequences between drone collision and bird strike can be considered for two reasons. First, the bird material was fluid-like would splash during the collision so that increasing the contact area and decrease impact loading. In other words, the stress distribution due to bird strikes is wider than the drone collision. In a bird strike problem, the energy absorbed by the deformation of the aircraft structure is 5.9% greater than that of a drone collision as shown in Figure 3-10 and the bird does not penetrate the aircraft structure. However, the drone component showed solid characteristics during the collision process. The impact load was more concentrated which is indicated by the maximum plastic strain only in the failure area. Additionally, the impact load caused a local fracture of the skin and then cause large penetration due to crack propagation. From the above discussion, it can be assumed that hardness plays an important role rather than kinetic energy which is the biggest difference between drone collisions and bird strikes.

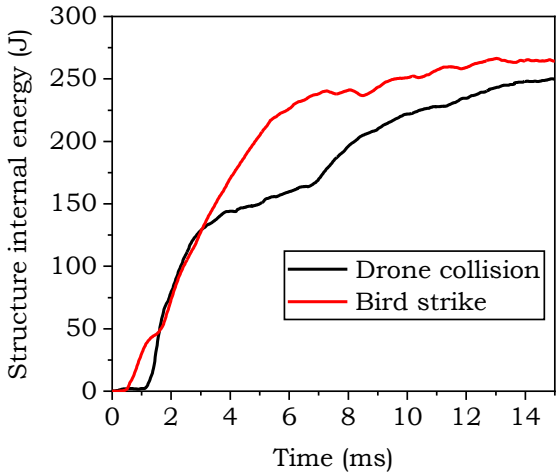

Figure 3-10: Aircraft structure internal energy

4. Conclusions

This research was performed to analyze drone and bird collision against aircraft commuter wing section. When a drone airborne collision occurs at the aircraft maximum approach flap speed and cruising speed, the commuter aircraft is in unairworthy condition. In other words, the commuter aircraft cannot complete the flight safely. This condition is caused by damage to the wing front spar and fire risk of the lithium-ion battery. The thickness of the skin, spar, and rib have been proven ineffective against drone airborne collisions so that increasing the thickness was needed. Drone collision

would cause more serious consequences than a bird strike at the same mass, the drone can easily penetrate the skin and cause damages to the primary structures of the aircraft. Therefore, relevant airworthiness standards should be drafted to ensure the safe operation of the aircraft.

Acknowledgments

This research was supported by Mr. Prio Adhi Setiawan as a Senior Advisor at the German Indonesian Association of Experts and Scholars. S

References

Barber, J. P., & Wilbeck, J. S. (1987). *Bird impact loading. The Shock and vibration bulletin Part 2. 48*.

Dar, U. A., Zhang, W., & Xu, Y. (2013). FE analysis of dynamic response of aircraft windshield against bird impact. *International Journal of Aerospace Engineering*, *2013*. https://doi.org/10.1155/2013/171768

FAA. (1993). *FAR 91.117 Aircraft speed. 18334*.

FAA. (2016). Small Unmanned Aircraft Systems (sUAS) Part 017. *Area*, *January*, 1–4.

Hedayati, R., & Sadighi, M. (2015). Bird Strike: An Experimental, Theoretical and Numerical Investigation. In *Woodhead Publishing*. https://doi.org/10.1016/C2014-0-02336-2

Hedayati, R., & Ziaei-Rad, S. (2013). A new bird model and the effect of bird geometry in impacts from various orientations. *Aerospace Science and Technology*, *28*, 9–20. https://doi.org/10.1016/j.ast.2012.09.002

Heimbs, S. (2011). Computational Methods for Bird Strike Simulations: A Review. *Computers and Structures*, *89*(23–24), 2093–2112. https://doi.org/10.1016/j.compstruc.2011.08.007

Jenkins, D., & Vasigh, B. (2013). The Economic Impact of Unmanned Aircraft Systems Integration in the United States. In *Association for Unmanned Vehicle Systems International*.

Liu, J., Li, Y., & Gao, X. (2014). Bird strike on a flat plate: Experiments and numerical simulations. *International Journal of Impact Engineering*. https://doi.org/10.1016/j.ijimpeng.2014.03.006

Lu, X., Liu, X., Li, Y., Zhang, Y., & Zuo, H. (2020). Simulations of airborne collisions between drones and an aircraft windshield. *Aerospace Science and Technology*. https://doi.org/10.1016/j.ast.2020.105713

Meng, X., Sun, Y., Yu, J., Tang, Z., Liu, J., Suo, T., & Li, Y. (2019). Dynamic response of the horizontal stabilizer during UAS airborne collision. *International Journal of Impact Engineering*. https://doi.org/10.1016/j.ijimpeng.2018.11.015

Millan, R. M., von Steiger, R., Ariel, M., Bartalev, S., Borgeaud, M., Campagnola, S., Castillo-Rogez, J. C., Fléron, R., Gass, V., Gregorio, A., Klumpar, D. M., Lal, B., Macdonald, M., Uk Park, J., Sambasiva Rao, V., Schilling, K., Stephens, G., Title, A. M., & Wu, J. (2019). Small Satellites for Space Science. *Advances in Space Research*. https://doi.org/10.1016/j.asr.2019.07.035

Republic Indonesia Ministry of Transportation. (2014). *Civil Aviation Safety Regulation Part 23 amdt1 Airworthiness Standard: Normal, Utility, Acrobatic, and Commuter Category Airplanes*. 1–272.

Sahraei, E., Hill, R., & Wierzbicki, T. (2012). Calibration and finite element simulation of pouch lithium-ion batteries for mechanical integrity. *Journal of Power Sources*. https://doi.org/10.1016/j.jpowsour.2011.10.094

Sahraei, E., Meier, J., & Wierzbicki, T. (2014). Characterizing and modeling mechanical properties and onset of short circuit for three types of lithium-ion pouch cells. *Journal of Power Sources*. https://doi.org/10.1016/j.jpowsour.2013.08.056

Schroederi, K., Song, Y., Horton, B., & Bayandor, J. (2017). Investigation of UAS ingestion into high-bypass engines, Part II: Drone parametric study. *58th AIAA/ASCE/AHS/ASC Structures, Structural Dynamics, and Materials Conference, 2017*.

SIMULIA. (2011). *A Strategy for Bird Strike Simulations using Abaqus / Explicit* (Issue Dassault Systems Online Support Document, Answer ID-4493 (Best Practices for Bird Strike Analysis)).

Smojver, I., & Ivančević, D. (2012). Advanced modelling of bird strike on high lift devices

using hybrid Eulerian-Lagrangian formulation. *Aerospace Science and Technology*. https://doi.org/10.1016/j.ast.2011.07.010

Song, Y., Horton, B., & Bayandor, J. (2017). Investigation of UAS ingestion into high-bypass engines, Part I: Bird vs. drone. *58th AIAA/ASCE/AHS/ASC Structures, Structural Dynamics, and Materials Conference, 2017*. https://doi.org/10.2514/6.2017-0186

Waqas, H. M., Shi, D., Imran, M., Khan, S. Z., Tong, L., e Ahad, F., Zaidi, A. A., Iqbal, J., & Ahmed, W. (2019). Conceptual design of composite sandwich structure submarine radome. *Materials*. https://doi.org/10.3390/ma12121966

Wilbeck, J. S. (1978). *Impact Behavior of Low Strength Projectiles. Technical Report AFML-TR-77-134. Air Force Materials Laboratory. Wright-Patterson Air Force Base*, *Ohio*, *45433*, *USA*.

.